Optimising the sensing volume of OPM sensors for MEG source reconstruction

Bezsudnova, Yulia; Koponen, Lari; Barontini, Giovanni; Jensen, Ole; Kowalczyk, Anna

DOI:
10.1016/j.neuroimage.2022.119747

Document Version
Publisher's PDF, also known as Version of record

Citation for published version (Harvard):
Bezsudnova, Y, Koponen, L, Barontini, G, Jensen, O & Kowalczyk, A 2022, 'Optimising the sensing volume of OPM sensors for MEG source reconstruction', *NeuroImage*, vol. 264, 119747.
https://doi.org/10.1016/j.neuroimage.2022.119747

NeuroImage 264 (2022) 119747

Contents lists available at ScienceDirect

NeuroImage

journal homepage: www.elsevier.com/locate/neuroimage

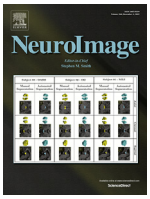

Optimising the sensing volume of OPM sensors for MEG source reconstruction

Yulia Bezsudnova[a], Lari M. Koponen[b], Giovanni Barontini[a,b], Ole Jensen[b], Anna U. Kowalczyk[b,*]

[a] School of Physics and Astronomy, University of Birmingham, Edgbaston, Birmingham, B15 2TT, United Kingdom
[b] Centre for Human Brain Health, School of Psychology, University of Birmingham, Edgbaston, Birmingham, B15 2SA, United Kingdom

ARTICLE INFO

Keywords:
Optically pumped magnetometers
Magnetoencephalography
Quantum sensors
Optimisation
Source reconstruction
Sensing volume

ABSTRACT

Magnetoencephalography (MEG) based on optically pumped magnetometers (OPMs) has been hailed as the future of electrophysiological recordings from the human brain. In this work, we investigate how the dimensions of the sensing volume (the vapour cell) affect the performance of both a single OPM-MEG sensor and a multi-sensor OPM-MEG system. We consider a realistic noise model that accounts for background brain activity and residual noise. By using source reconstruction metrics such as localization accuracy and time-course reconstruction accuracy, we demonstrate that the best overall sensitivity and reconstruction accuracy are achieved with cells that are significantly longer and wider that those of the majority of current commercial OPM sensors. Our work provides useful tools to optimise the cell dimensions of OPM sensors in a wide range of environments.

1. Introduction

Magnetoencephalography (MEG) provides a powerful non-invasive tool for neuroimaging. Conventional MEG systems consist of arrays of hundreds of pick-up coils coupled to superconducting quantum interference devices (SQUIDs) and enable the reconstruction of neural activity with millisecond temporal precision (Hämäläinen et al., 1993) and millimeter resolution (Barratt et al., 2018). The requirement of cryogenics and thermal insulation, as well as lack of flexibility, are the main limiting factors for SQUIDs in biomagnetic measurements.

Optically pumped magnetometers (OPMs) (Budker and Romalis, 2007) are an alternative type of sensitive magnetometers with the potential to surpass the performance of superconducting sensors in brain imaging. Successful demonstrations of detection of human brain activity using various types of OPMs have been reported over the past years (Boto et al., 2018; Colombo et al., 2016; Johnson et al., 2010; Kamada et al., 2015; Kowalczyk et al., 2021; Osborne et al., 2018; Sander et al., 2012; Sheng et al., 2017; Xia et al., 2007). A number of works demonstrated that OPMs enable the study of previously difficult to detect biomagnetic signals in human and animal neurophysiology (Boto et al., 2018; Broser et al., 2018; Holmes et al., 2021; Jensen et al., 2016; Seymour et al., 2021; Tierney et al., 2021; Westner et al., 2021).

In OPMs the thermal insulation gap is in the mm range and, as a consequence, the sensors can be brought closer to the scalp and the brain than SQUIDs. Based on simulations, the neuromagnetic signal measured by an on-scalp OPM sensor is expected to be on average 5 times stronger than the one measured by a SQUID sensor. This can potentially lead to more accurate source reconstruction (Boto et al., 2016; Iivanainen et al., 2017; 2019). Despite this potential, so far the experimental results have only demonstrated OPM-MEG performance comparable to conventional SQUID-MEG systems (Borna et al., 2020; Hill et al., 2020; Iivanainen et al., 2020).

Recent works have studied various aspects of the performance of OPM-MEG systems, trying to unlock their full potential. Investigations focused on quantifying the dependence of neuronal source localisation accuracy on the number of sensors, their layouts (Beltrachini et al., 2021; Duque-Muñoz et al., 2019; Pratt et al., 2021; Riaz et al., 2017), improvement of information content acquired with multi-axial sensor arrays, (Brookes et al., 2021; Iivanainen et al., 2017) or accuracy of sensor positioning needed for precise source reconstruction (Hill et al., 2020; Zetter et al., 2018). Most of these works assumed fixed single-sensor response and noise models that are based on either idealized point-like sensors (Boto et al., 2016; Brookes et al., 2021; Clancy et al., 2021; Iivanainen et al., 2021) or sensors with arbitrary noise levels (Iivanainen et al., 2017).

It is of capital importance to consider that neuromagnetic fields decay with the square of the distance and an OPM sensor registers the signal averaged over its sensitive volume. Therefore, a smaller

* Corresponding author.
E-mail address: a.u.kowalczyk@bham.ac.uk (A.U. Kowalczyk).

https://doi.org/10.1016/j.neuroimage.2022.119747.
Available online 18 November 2022.

sensing volume results in higher recorded signal amplitude but also higher recorded brain noise. Furthermore, the size of the sensitive volume affects the intrinsic sensitivity of the sensor. Existing OPMs have cell sizes ranging from $1 \times 2 \times 3$ mm^3 in chip-scale sensors (Knappe et al., 2016) to bench-top sensors with 30 mm spherical cells (Acosta et al., 2006). So far, however, no exhaustive analysis has been carried out to determine the optimal sensing element dimensions for an OPM-MEG system.

In this work, we study how the dimensions of the OPM sensing element, namely its vapour cell, can be optimised depending on residual noise sources. We first concentrate on the optimisation of the performance of a stand-alone sensor, which can be useful for the development of prototype sensors. In this case, we determine the optimal dimensions by maximising the signal-to-noise ratio. We then consider arrays of sensors, determining their optimal sensing volume by optimising the ability of the array to localise a source and extract its time course.

2. Theory

This section is divided into two parts. The first part collects the equations that we use to study and optimise the dimensions of the vapour cell of a single OPM sensor; the second part describes the equations required to expand the analysis to an array of sensors.

2.1. Stand-alone OPM sensor

The core component of an OPM sensor is the vapour cell that contains the atomic gas, typically an alkali metal vapour. An OPM measures magnetic fields by measuring changes in the properties of light interacting with the atomic medium contained in its sensing volume, once this is exposed to such fields (Bell and Bloom, 1957). The performance of any magnetometer can be assessed by its signal-to-noise ratio,

$$SNR = \frac{S}{\delta \tilde{B}}, \tag{1}$$

where S is the signal amplitude detected by the sensor and $\delta\tilde{B}$ is the total amplitude of the recorded noise. In a perfectly shielded environment the value of $\delta\tilde{B}$ determines the sensitivity δB of the sensor in a given measurement bandwidth f_{BW}, $\delta B = \delta\tilde{B}/\sqrt{f_{\mathrm{BW}}}$[1]. In real conditions it is impossible to separate the external magnetic field fluctuations from the intrinsic noise of the sensor. Therefore, $\delta\tilde{B}$ can be expressed as:

$$\delta\tilde{B} = \sqrt{(\delta\tilde{B}_i)^2 + \tilde{N}^2} \tag{2}$$

with $\delta\tilde{B}_i$ the intrinsic noise of the sensor and $\tilde{N}$ the external magnetic field noise amplitude. There are two fundamental noise sources that determine the intrinsic sensitivity of an OPM:

$$\delta B_i = \sqrt{\left(\delta B_{\mathrm{at}}\right)^2 + \left(\delta B_{\mathrm{ph}}\right)^2}, \tag{3}$$

where δB_{at} is the atomic-shot noise and δB_{ph} is the the photon-shot noise. The expressions for these two terms are derived in Appendix A for both nonlinear magneto-optical rotation (NMOR) and spin-exchange relaxation-free (SERF) OPM sensors. In this work, we assume $f_{\mathrm{BW}} = 25$ Hz as that is sufficient to record oscillatory brain activity in the alpha and beta band.

The external magnetic field noise amplitude recorded by the sensor in MEG experiments can be expressed as:

$$\tilde{N} = \sqrt{\left(\tilde{N}_b\right)^2 + \left(\tilde{N}_r\right)^2}, \tag{4}$$

[1] Mind the notation: the sensitivity and the amplitude spectral density have units of fT/$\sqrt{\mathrm{Hz}}$ and is marked as δB_x. The noise amplitude, i.e. the standard deviation of the noise, in a given measurement bandwidth has units of fT and is marked with $\delta\tilde{B}_x = \delta B_x \cdot \sqrt{f_{\mathrm{BW}}}$. The same notation applies to N_x and $\tilde{N}_x$

where $\tilde{N}_b$ is the detected "brain noise", resulting from the background brain activity and $\tilde{N}_r$ is the residual magnetic field noise that accounts for the components of the environmental noise and sensor's technical noise that cannot be compensated for. The brain noise decreases with the distance from the head, therefore $\tilde{N}_b$ depends on the volume of the cell. The environmental noise originates from stray magnetic fields, thermal currents induced in the magnetically shielded room and vibrations of its walls, nearby electrical equipment, mechanical movement of magnetic or conductive components (e.g. elevators, urban traffic), and electrically active tissues. Such noise, generated by distant sources outside of the head, can be considered as spatially homogeneous (Tierney et al., 2021). The spatially and temporally correlated components of the environmental noise can be usually removed in data pre-processing by using various filtering methods such as signal space separation (SSS) (Seymour et al., 2021; Taulu and Kajola, 2005) or with magnetic field compensation systems (both require additional reference sensors). Advanced coils, such as those described in (Holmes et al., 2019), can attenuate the dominant components of the static background field as well as their first order spatial gradients. Additionally, if used with feedback controllers, very low frequency magnetic field drifts can be significantly suppressed. However, such compensation can introduce magnetic noise in other frequency bands. In addition, every OPM sensor is subject to technical noise arising from fluctuations in the laser light intensity, frequency and polarization fluctuations, atomic cell temperature fluctuations, current noise, and other various electronic noises that can affect the magnetometer readout (Krzyzewski et al., 2019). In our simulations, $\tilde{N}_r$ accounts for every technical and residual noise that cannot be actively or passively compensated. We additionally consider $\tilde{N}_r$ as white noise in the spectral interval 4–100 Hz (Vrba and Robinson, 2002). In line with state-of-the-art methods like those developed in (Handy, 2005; Marhl et al., 2022a; Seymour et al., 2021), we assume that the noise below 4 Hz is filtered out, therefore our measurement bandwidth is 5-30 Hz. In this work, $\tilde{N}_r$ is used as a free parameter with the standard deviation ranging from 0 to 100 fT, similarly to (Iivanainen et al., 2019).

2.1.1. Forward model for an OPM sensor

Our signal of interest, S, and brain noise, $\tilde{N}_b$, are due to the magnetic field arising from the neural activity in the brain. This neural activity gives rise to a primary current distribution and we approximate it with a set of equivalent current dipoles (ECDs) inside the brain. We obtain the associated magnetic field from a spherical volume conductor model of the head, identical to the one in (Hämäläinen et al., 1993). We approximate the signal S with one tangential source ECD and the brain noise with a set of independent, tangential and randomly oriented ECDs (Iivanainen et al., 2017; Kemppainen and Ilmoniemi, 1989; Marhl et al., 2022b; Vrba and Robinson, 2002).

As mentioned, an OPM produces a signal that is proportional to the mean magnetic field measured within the sensing volume (Budker and Romalis, 2007). For NMOR sensors, that typically use paraffin coated cells, this volume is determined by the glass cell volume, while for SERF sensors, that employ buffer gas cells, sensing volume is the intersection between the cell volume and the probe laser beam. Therefore the signal of interest is

$$S = \frac{1}{V}\int_V \vec{B}_{sECD}\left(\vec{r}\right)\cdot\vec{n}\ \ dV, \tag{5}$$

where $V = L \times D^2$ is the volume of the vapour cell with length L and the cross-section D^2, $\vec{B}_{sECD}$ is the magnetic field produced by the source ECD, and $\vec{n}$ is the measurement axis of the OPM. Similarly, the brain noise is the net signal generated by a set of randomly oriented dipoles:

$$\tilde{N}_b = \mathrm{RMS}_{100}\left[\sum_j \frac{1}{V}\int_V \vec{B}_{ECD,j}(\vec{r})\cdot\vec{n}\ dV\right], \tag{6}$$

where the index j runs over the dipoles. The noise amplitude is obtained by generating 100 of such sets and calculating the root mean square of

the computed sums. The modeled system is shown in Fig. 1. The head is approximated with a conductive sphere with radius $R_{\text{head}} = 91$ mm and the brain with a concentric sphere with radius $R_{\text{brain}} = 80$ mm. The signal S arises from a single tangential 10 nAm dipole, and $\tilde{N}_b$ from 1000 randomly oriented dipoles (0.2 nAm each). For such model, the forward problem has a closed-form solution (Sarvas, 1987) and we obtain realistic values for the signal of interest and brain noise.

We define L_{opt} and D_{opt} as optimal length and width that yield the highest value of SNR at given N_r. Our procedure to find L_{opt} and D_{opt} for a single OPM sensor is the following: (i) we generate a randomly oriented tangential source dipole at a given depth ($\Delta = 20$–45 mm) and adjust the angle between the OPM sensing axis and the dipole ϕ (see Fig. 1) to maximise S. (ii) we generate 1000 randomly uniformly oriented and positioned ECDs inside the brain. (iii) we add white residual noise N_r and intrinsic noise $\delta\tilde{B}_i$. (iv) we search for the highest SNR scanning the sensor dimensions L and D. This procedure is repeated for 100 trials. For each set of dimensions we calculate $\delta\tilde{B}_i$ using the parameters listed in Appendix A. All computations are performed using the FieldTrip toolbox (Oostenveld et al., 2011) and custom MATLAB scripts (R2019b, Mathworks, USA). We have verified that our model reproduces typical values. For an ideal noise-free point-like SQUID sensor placed 40 mm above the scalp, $N_r = 5\ fT/\sqrt{\text{Hz}}$, and Δ =2.1 cm, we obtain SNR ≈ 1.9, which is within the range of typical MEG data (Jaiswal et al., 2020).

2.2. An array of OPM sensors

We estimate the performance of an OPM-MEG system, consisting of an array of sensors, using its source localisation accuracy and time course reconstruction accuracy. A quasi-uniform array of sensors over one of the hemispheres of a spherically symmetric head model reaches best localisation accuracy with a finite number of sensors, depending on the amplitudes of both the brain noise $\tilde{N}_b$ and the signal of interest S (Vrba and Robinson, 2002). In this work, we define the optimum number of sensors as the minimum number of sensors that enables best localisation accuracy. Assuming that each sensor in the array has an identical sensing volume, we perform an exhaustive search over L and D to maximise the source reconstruction accuracy. For these calculations, $\tilde{N}_r$ is set to 25 fT, corresponding to N_r= 5 fT/$\sqrt{\text{Hz}}$. As long as the dimensions of the sensitive volume of each sensor are much smaller than the spacing between adjacent sensors, the spatial sampling of an array of sensors (Ahonen et al., 1993) is limited by the sensor spacing and not by dimensions of the sensitive volume. This greatly simplifies the problem because it is sufficient to optimise the sensitive volume to accurately reconstruct a single ECD, rather than modeling the general case of two or more partially correlated sources.

2.2.1. Localisation accuracy

We define the localisation accuracy for a single dipolar source as the volumetric error

$$\sigma_V = \sqrt{(\sigma_x)^2 + (\sigma_y)^2 + (\sigma_z)^2}, \tag{7}$$

where σ_i is the root mean square (RMS) error of the reconstructed dipole position in the direction i (Vrba and Robinson, 2002). To avoid overfitting due to exactly ideal forward model, we introduce trial-by-trial inaccuracy to sensor positions and orientations. When measuring the field and the brain noise, each sensor has a uniform random offset (RMS 4 mm) and a uniform random tilt (RMS 9°) from the normal to the head orientation, corresponding to the suggested co-registration accuracy of an OPM-MEG system by (Zetter et al., 2018). Our procedure in this case is the following: (i) we generate a random tangential ECD in a random position ($\Delta = 21$–26 mm) and 1000 randomly oriented ECDs inside the brain. (ii) we compute the signal and brain noise recorded by the inaccurately positioned sensor array (100 sets). (iii) we add white residual and intrinsic noise. (iv) assuming the ideal sensor locations, we reconstruct a single dipole using a dipole fitting algorithm[2]. For each array of sensors, the localisation procedure was performed for 9 ECD dipole positions, repeated 100 times for different sensor location errors and noise $\tilde{N}$. We do maintain the correct spatial relationship between the sources and the generated brain noise.

2.2.2. Time course reconstruction accuracy

The ability to localise a dipolar source does not reveal the full picture of the performance of an array of sensors, as such reconstruction has very low sensitivity to uncorrelated noise. Thus, to better assess the performance, we also compute the time course prediction error E_{tot}, a metric that estimates the ability of the array to reconstruct the temporal waveform of a dipolar source using a beamformer analysis (Brookes et al., 2008).

As our MEG model includes spatially correlated brain noise, we cannot use the closed-form solution of E_{tot} derived by (Brookes et al., 2021). Instead we estimate E_{tot} as

$$E_{tot} = \frac{1}{M}\sqrt{\sum_{i=1}^{M}\left(\hat{q}_i - q_i\right)^2}, \tag{8}$$

where $M = 10,000$ is the number of time points, $\hat{q}_i$ is the estimated source magnitude, and q_i is the true source magnitude at time i. Here,

$$\hat{q}_i = \boldsymbol{\omega}^\top \boldsymbol{b}_i, \tag{9}$$

where $\boldsymbol{\omega}$ is the filter to extract $\hat{q}_i$ from the measurement $\boldsymbol{b}_i$. Given that

$$\boldsymbol{\omega} = \underset{\boldsymbol{\omega}}{\operatorname{argmin}}\ E\left(\hat{q}_i^2\right)\ \text{ while }\ \boldsymbol{\omega}^\top \boldsymbol{l} = 1, \tag{10}$$

where $E(\cdot)$ is the expected value and $\boldsymbol{l}$ is the lead field of the source. A closed-form solution is (Van Veen et al., 1997):

$$\boldsymbol{\omega} = \frac{\boldsymbol{l}^\top \mathbf{C}^{-1}}{\boldsymbol{l}^\top \mathbf{C}^{-1}\boldsymbol{l}}, \tag{11}$$

where C is the data covariance matrix.We use the exact C as the sum of contributions from the source, all of the 1000 noise dipoles, N_r and δB_i. For each dipole $\mathrm{C}^* = (q^*_{\text{RMS}})^2 \cdot l^* l^{*\top}$, where q^*_{RMS} is the root mean square of the amplitude of the relevant dipole (marked with *) over time. While the contribution from all the other noise sources is given by $\mathrm{C}^* = \mathrm{s} \cdot \mathrm{I}$, where s is a standard deviation of the relevant noise term and I is the identity matrix. To reduce random variability, we show the root-mean-square value of 9 E_{tot} estimates for random source dipoles located 21–26 mm from the head surface. For each source, similarly to (Brookes et al., 2021), we assume that the exact $\boldsymbol{l}$ is known.

3. Results

3.1. Optimal sensing volume for a stand-alone OPM sensor

For both NMOR and SERF sensors, L is the length of the cell along the sensitive direction. For NMOR, D^2 is the cross-section of the cell, whereas, for SERF, D^2 is the cross-section of the laser beam. We impose 0.2 cm $\leqslant L_{opt} \leqslant$ 5 cm and 0.2 cm $\leqslant D_{opt} \leqslant$ 2 cm, to be compatible with the majority of cell production processes.

In general, both the recorded signal S and the brain noise degrade with L because the sensor is averaging over regions increasingly far from the scalp. The intrinsic sensitivity δB_i is instead lower for larger sensing volumes (Fig. A.1). S, δB_i, $\tilde{N}_b$ decrease with different scaling with L and D. Fig. 2a– d show the optimal dimensions L_{opt} and D_{opt} as a function

[2] We are using the dipole fitting function ft-dipolefitting in FieldTrip, that assumes a spherical head model(Oostenveld et al., 2011)

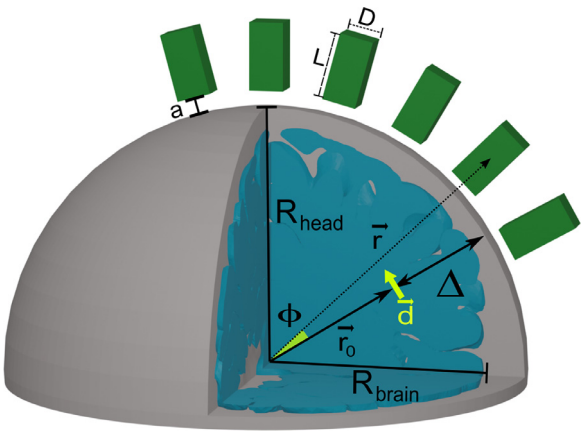

Fig. 1. The model. The radius of the head is R_{head} and the radius of the brain is R_{brain}. An equivalent current dipole tangential to the head surface is positioned at point $\vec{r}_0$ inside the brain and has a moment $\vec{d}$. The distance between the head surface and the dipole is Δ. A sensor with a rectangular cuboid cell positioned at $\vec{r}$ is measuring a signal S from the dipole. The cuboid has length L in the radial direction and D in both tangential directions and is away from the head by distance a. The angle between $\vec{r}_0$ and $\vec{r}$ is ϕ.

of the residual noise N_r for few depths of the ECD Δ. For superficial sources (Δ < 35 mm), as L increases the signal decreases faster than the brain noise, and thus the optimal length varies between 0.6–1.1 cm for NMOR (Fig. 2a) and 0.2–0.3 cm for SERF (Fig. 2b). Whereas for deeper sources (Δ > 35 mm) the brain noise averages out faster than the signal of interest. Therefore, for the low-noise regime (up to 5 fT/$\sqrt{\text{Hz}}$), the optimal cell length changes faster with N_r for deeper sources than for the superficial ones. This effect is stronger for the SERF sensor (Fig. 2b), which has lower intrinsic noise level. In the limit of high residual noise (10 fT/$\sqrt{\text{Hz}}$), the optimal sensor length decreases. This is because the residual noise is independent of the cell size.

The magnetic field distribution at a given distance a outside of the head is relatively smooth, i.e, the magnetic field around the optimal sensor location is approximately constant (refer to topographic maps of typical MEG data). Thus, increasing D improves the sensor's sensitivity by reducing δB_i. For example, an increase of D from 0.2 cm to the maximum allowed 2 cm reduces δB_i by 50% for NMOR and by 90% for SERF (Appendix A), while keeping S and $\tilde{N}_b$ are almost constant. Overall, wider sensors (D > 1 cm) record higher SNR and better detect deep sources (Fig. 2c– d).

In Fig. 2e-f we show the signal-to-noise ratio SNR as a function of residual noise N_r for L_{opt} and D_{opt} for the same depths of ECD Δ. For NMOR (SERF) sensors, the best SNR is 7 (13), obtained for superficial sources in low noise environment. This decreases to 1.5 (2) for deep sources and high N_r. The lower intrinsic noise of SERF is a significant advantage in a single sensor arrangement. Note that in our simulations, the gap between the head surface and the sensing volume a is the same for both sensors. In practice, this gap might be few mm larger for SERF since such sensor requires hot vapour cells and thermal insulation, which will have a significant effect on SNR.

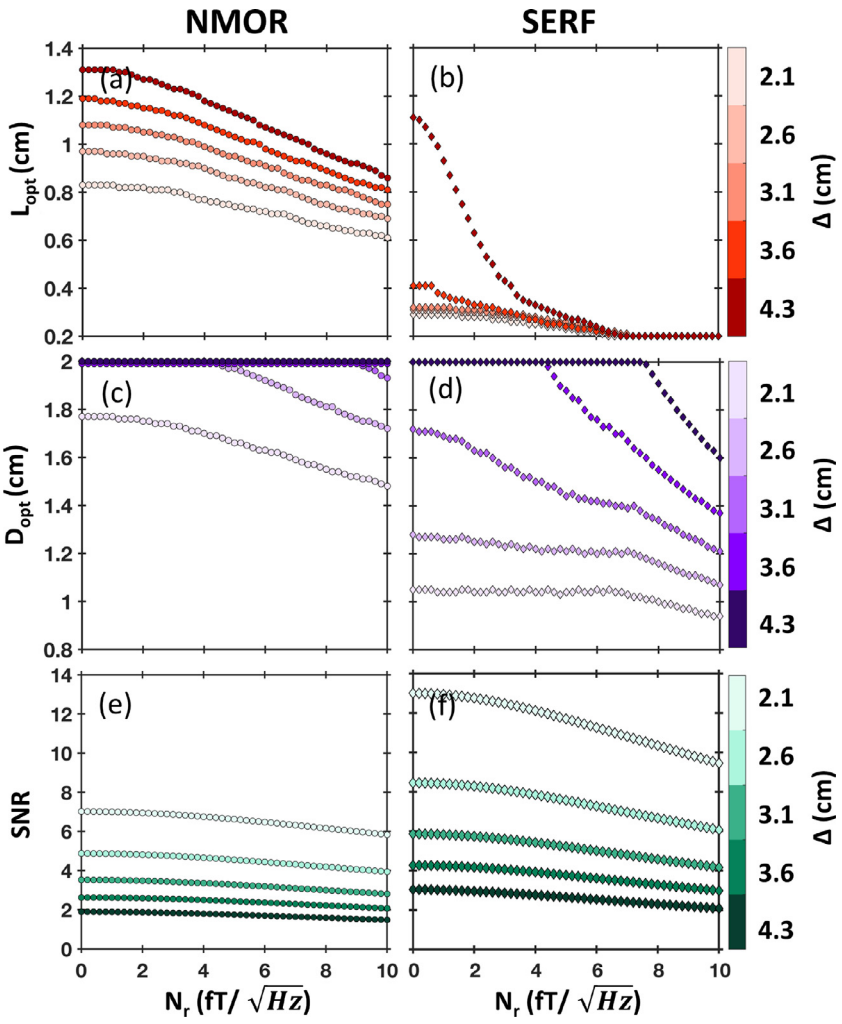

Fig. 2. Optimal sensing element dimensions for a single OPM sensor calculated for various depths of ECD Δ, f_{BW} =25 Hz. Optimal length L_{opt} for corresponding D_{opt} as a function of residual noise N_r for NMOR sensor (a) and for SERF sensor (b); optimal diameter D_{opt} for corresponding L_{opt} as a function of N_r for NMOR sensor (c) and for SERF sensor (d); SNR for corresponding L_{opt} and D_{opt} for NMOR sensor (e) and for SERF sensor (f).

Fig. 2 serves as a guideline for choosing the optimal sensing volume dimensions depending on the experimental conditions if the number of sensors is very limited. Also, it illustrates that L and D have a clear optimal value corresponding to the balance point between how well each sensor is measuring the ECD and how well it is averaging the noise out.

3.2. Optimal number of OPM sensors

To evaluate the optimal number of sensors in an array, we carried out two sets of simulations. The first set, marked as $av = 1$ in Fig. 3a and Fig. 4 rows 1 and 2, is a real-time measurement where simulated data corresponds to a single epoch. The second, marked as $av = 20$ in Fig. 3b and Fig. 4 rows 3 and 4, simulates data averaged over 20 epochs. The epochs are generated for each of the 100 noise and sensors location error sets (see Section 2.2.1). As we show later, averaging over 20 epochs reduces the noise to the level, delivering almost perfect source localisation with $\sigma_V \leqslant 4$ mm. In Fig. 3a– b, we show the localisation accuracy of a dipole placed at Δ=2.1 cm in the presence of residual noise $N_r = 5$ fT/$\sqrt{\text{Hz}}$ calculated for $L_{opt} = 0.7$ cm, $D_{opt} = 1.7$ cm for NMOR sensors, and $L_{opt} = 0.2$ cm, $D_{opt} = 1$ cm for SERF sensors. For comparison, we are also showing the localisation accuracy obtained for arrays of SQUID magnetometers. Calculations are performed for both sets, $av = 1$ (Fig. 3a) and $av = 20$ (Fig. 3b), using the procedure described in section 2.2.1. In this case, the point-like sensors are placed 4 cm from the head surface (Boto et al., 2016; Vrba and Robinson, 2002).

To evaluate the optimal number of sensors for a time-course reconstruction, we find the minimum E_{tot} over all the possible sensors dimensions for a given number of sensors, as shown in Fig. 3c. In Fig. 3d and e, we report the corresponding L and D. The shaded coloured areas in Fig. 3d– e mark the range of dimensions where E_{tot} is within 5% of this minimum. For NMOR the corresponding D overlaps with the largest possible width for the considered number of sensors in an array. From our results it emerges that for an on-scalp OPM-MEG system with optimized sensor dimensions, the optimal number of sensors in an array is about 70. This is because this is the minimum number to reach a plateau in both σ_V and E_{tot}, indicating that no significant gain in localisation is achieved by adding more sensors. This number is slightly lower than the 100 sensors required to meet the same criteria for a conventional off-scalp MEG. (Vrba and Robinson, 2002).

3.2.1. Optimal vapour cell dimensions in an array

In Fig. 4 we show how the source reconstruction accuracy depends on the sensing volume dimensions in the presence of brain noise for various powers of the residual noise. We perform the calculations for an array of 69 sensors. We choose this number because it is the closest to 70 (the optimal number derived in Section 3.2) that allows the algorithm we use to equidistantly space the sensors and cover the whole upper hemisphere (Deserno, 2004). In Fig 4, column A represents a noise-free sensor in perfect environment $\tilde{N}_r = 0$ fT. Column B shows low-noise regime $\tilde{N}_r = 25$ fT, which represents e.g. $N_r = 5$ fT/$\sqrt{\text{Hz}}$ at measurement bandwidth of $f_{\text{BW}} = 25$ Hz, conditions we chosen to investigate optimal number of sensors discussed in the previous section. Columns C and D with $\tilde{N}_r$=50 fT and $\tilde{N}_r$=100 fT respectively represent high residual noise regime.

Fig. 4 rows 1 and 2 show how σ_V depends on the sensing volume dimensions in the case of real-time experiments, av=1. In the low residual noise regime (column B), the optimal dimensions are 0.2 cm $\leqslant L_{opt} \leqslant$ 2 cm, 0.7 cm $\leqslant D_{opt} \leqslant$ 1.6 cm for NMOR and 0.2 cm $\leqslant L_{opt} \leqslant$ 4 cm, 0.5 cm $\leqslant D_{opt} \leqslant$ 1.6 cm for SERF. With increasing amplitude of the residual noise (columns C and D), the optimal length decreases while the optimal diameter of the sensor increases. The optimal dimensions in this regime are 0.3 cm $\leqslant L_{opt} \leqslant$ 1 cm, $D_{opt} \geqslant$ 1.2 cm for NMOR and

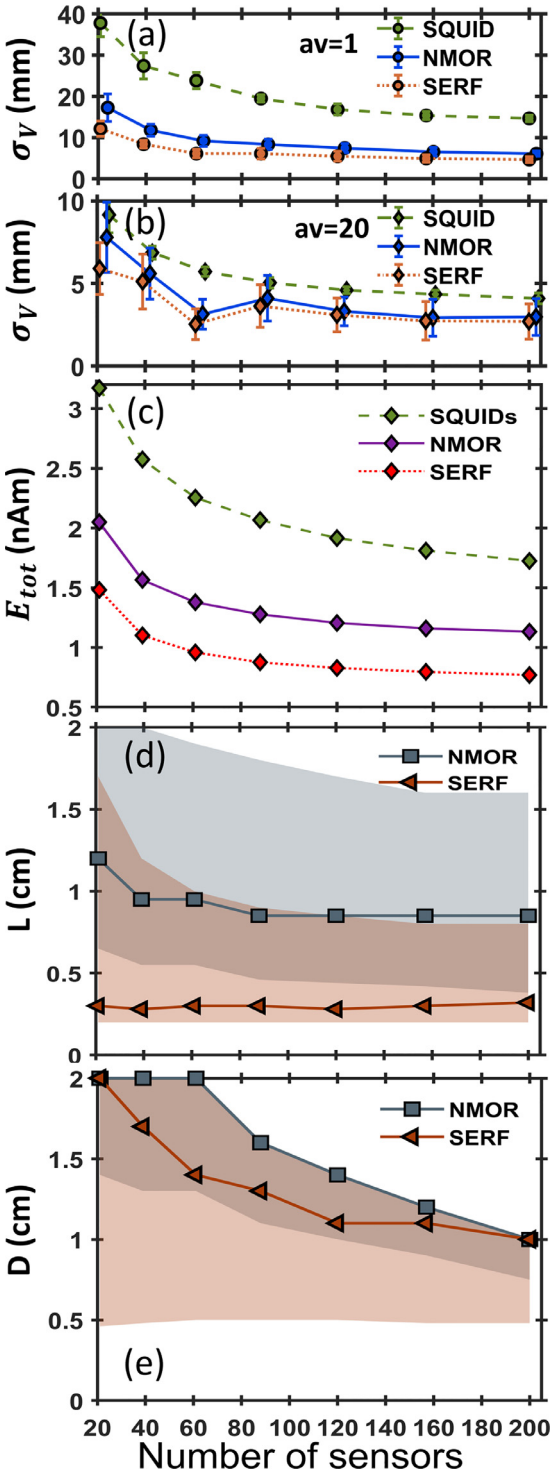

Fig. 3. Source reconstruction accuracy of a multi-sensor array in the presence of $\tilde{N}_b$ and $N_r = 5$ fT/$\sqrt{\text{Hz}}$. (a–b) Localisation accuracy σ_V as a function of the number of sensors for three exemplar arrays: Blue colour is for an NMOR OPM array with sensor dimensions set to $L = 0.7$ cm and $D = 1.7$ cm, orange colour is for SERF OPM array with sensor dimensions set to $L = 0.2$ cm and $D = 1$ cm. Green colour is for SQUID-MEG system with point-like magnetometers 40 mm from the head. (a) Single time-point data $av = 1$, (b) averaged 20 epochs data $av = 20$. (c) Minimum time course reconstruction accuracy E_{tot} as a function of the number of sensors in NMOR OPM array (purple), SERF OPM array (yellow) and SQUIDs array (green). (d–e) Respectively: corresponding L and D as a function of the number of sensors. The shaded area (grey - NMOR, red - SERF) marks the range of dimensions over which E_{tot} is within 5% of its minimum.

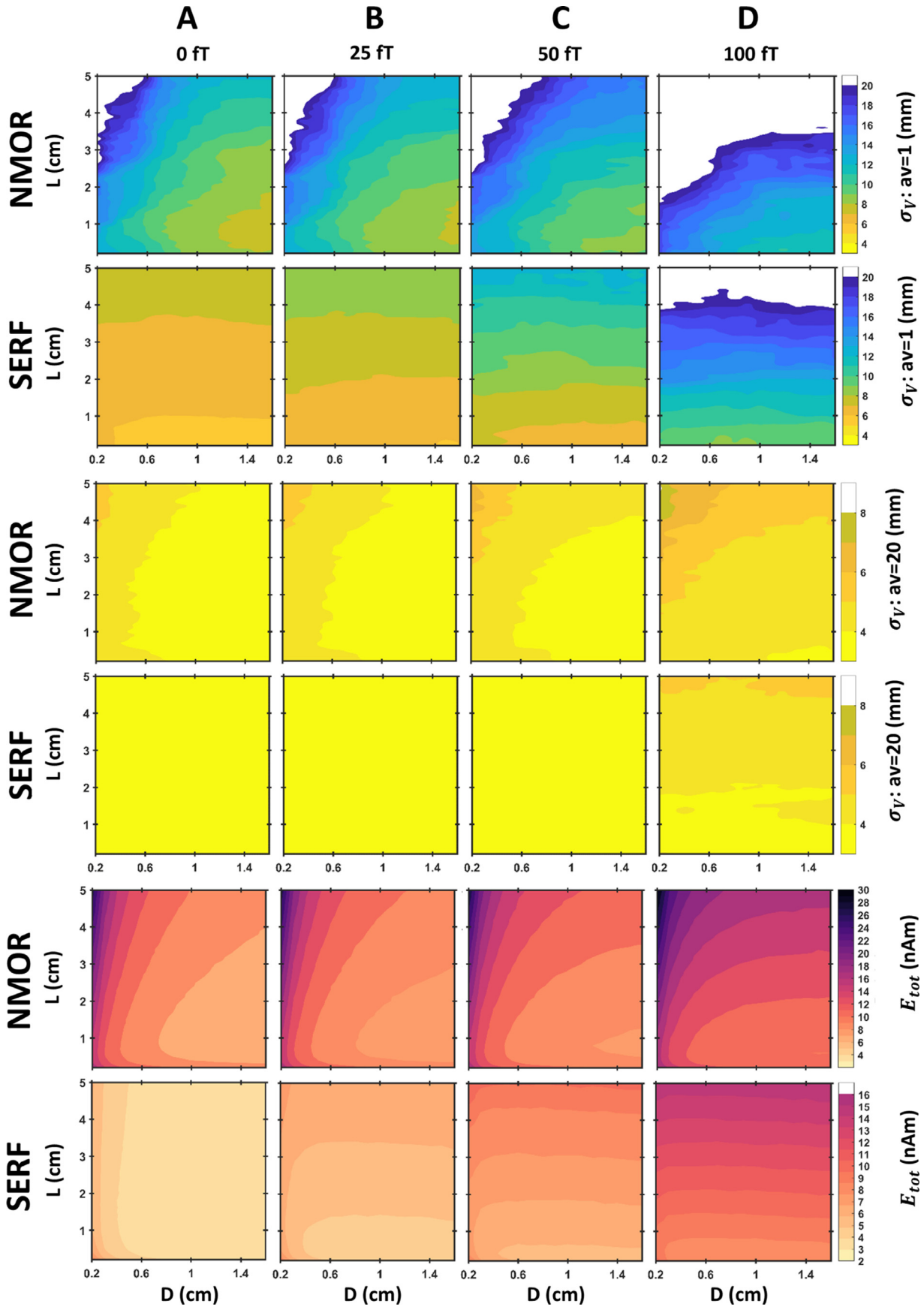

Fig. 4. Source reconstruction accuracy as a function of L and D in the presence of brain noise $\tilde{N}_b$ with residual noise standard deviation set to $\tilde{N}_r$ =0 fT (column A), $\tilde{N}_r$ =25 fT (column B), $\tilde{N}_r$ =50 fT (column C) and $\tilde{N}_r$ =100 fT (column D). Localisation accuracy σ_V in real-time experiment (av =1) for NMOR (row 1) and SERF (row 2) sensor array. σ_V in averaged experiment (av =20) for NMOR (row 3) and SERF (row 4) sensor array. Time course reconstruction accuracy E_{tot} for NMOR (row 5) and for SERF sensors array (row 6). White areas in rows 1 and 2 correspond to a failed source localization. Simulations are performed for an array formed by 69 sensors.

0.2 cm $\leqslant L_{opt} \leqslant$ 0.6 cm, $D_{opt} \geqslant$ 0.5 cm for SERF. The white area indicates regions where the source reconstruction algorithm could not converge and the ECD could not be localised. This happens when SNR$\leqslant$1.

In the *av*=20 set (Fig. 4 rows 3 and 4), D has almost no effect on σ_V in the residual noise limit of 50 fT (columns A–C) for both types of sensors. NMOR arrays with $D > 0.8$ cm and $L < 4$ cm, as well as all investigated SERF arrays, reach the best localisation accuracy ($\sigma_V \leqslant 4$ mm). The lower limit on the volumetric error is defined by the uncertainty in the sensors location. The geometrical errors are not affected by the dimensions of the sensor. In the high residual noise regime (column D), this limit is achieved only by SERF sensors with $L \leqslant 1$ cm and a narrow range of NMOR sensors ($D > 1$ cm and $L < 0.5$ cm). In all cases, σ_V is better for SERF since it has lower intrinsic noise level. Considering however sensors with optimal dimensions, the difference in σ_V between SERF and NMOR is significantly reduced. In Fig. 4 rows 5 and 6 we show how E_{tot} depends on the sensing volume dimensions. In low noise limit For NMOR arrays we observe a minimum for sensors with $L \approx 1$ cm and $D \geqslant 0.6$ cm. For SERF arrays, the minimum is obtained for $L \leqslant 1.3$ cm and $D \geqslant 0.4$ cm. For higher residual noise with a standard deviation of 50 fT, E_{tot} is stronger for $D > 1.2$ cm and 0.5 cm $L < 1$ cm in the case of NMOR and for $D > 0.5$ cm and $L < 0.5$ cm in case of SERF. When the residual noise becomes higher than the intrinsic noise level of the sensor, the dependency of σ_V and E_{tot} on the sensor diameter is lifted and the best performance is obtained with the shortest cells.

Our results show that OPM sensors achieve the best performance when the width of their sensing volume is the maximum allowed by the constraint of filling the whole head surface. For both sensor types, the smallest sensors have better localisation accuracy, but relatively weak time-course reconstruction. In summary, NMOR and SERF arrays perform best when their sensing elements have $L_{opt} \approx 0.2$–1 cm and $D_{opt} \geqslant 1$ cm for NMOR $D_{opt} \geqslant 0.6$ cm for SERF. This stands for real-time and averaged data.

4. Discussion

In this work, we presented a model to optimise the dimensions of the sensing volume of an OPM sensor for MEG. This optimisation yields the sensing volume that delivers the best performance in a realistic scenario where both residual noise and background brain activity are present. Our model can be used as a toolkit for optimizing the design of optically pumped magnetometers in given experimental conditions. Our results show that the dimensions of the sensing element are a significant parameter to take into account while designing single OPMs or whole-head OPM-MEG systems.

Our simulations demonstrate that the optimal size of a single sensor is similar to the optimal size of a sensor in an array. This can be understood considering that the magnetic field pattern produced by a ECD outside the head features two extrema, whose magnitude and spatial distribution depend on the ECD position and orientation. Usually, only a few sensors in the array are covering the area of these maxima. Thus, the sensors required to form an optimal array have dimensions roughly similar to those of a stand-alone sensor. However, even if arrays with very few sensors can record the signal of interest with good SNR, they will not perform well in source reconstruction experiments (as one can extrapolate from Fig 3 a–b). To effectively sample the brain signal and avoid aliasing of noise coming from non-compensated sources, larger arrays are needed. Our simulations show that the optimal number of sensors in an array is around 70. Such an array reaches the best reconstruction accuracy and can directly quantify the topography of the magnetic fields produced in the brain as well as perform analysis of the recorded signals at the sensor level.

It is worth noticing that most of commercial OPM sensors have cubic cells with a side of 0.2-0.3 cm and operate in SERF regime. The intrinsic noise level of commercial sensors is calculated to be around a few fT/$\sqrt{\text{Hz}}$. The actual sensitivities (≈10 fT/$\sqrt{\text{Hz}}$) are usually not limited by fundamental noise sources, but rather by technical noise sources (Krzyzewski et al., 2019). Columns C and D are the closest to represent such conditions in the measurement bandwidth of $f_{\text{BW}} = 25$ Hz or $f_{\text{BW}} = 100$ Hz respectively. According to our model, such sensors work well for reconstructing the location of the ECD in an offline experiment, where there is a number of trials to average out the noise, but can improve the performance for the time-course of the ECD or in real-time experiments. In the low noise limit, the change from 0.2 cm to 1.6 cm in the width of the cell results in a 2-fold increase in the ability to extract the time course and the same increase in localization accuracy for single-trial experiments. Our simulations show that the dimensions of the sensor's sensitive element are an important parameter to consider. Such optimisation has the potential to further improve the gain OPM-MEG systems have over the conventional SQUID-MEG. Increasing the width of the cell in the range of diameters investigated in this manuscript has no significant effect on spatial frequency sampling or spatial resolution.[3] Therefore, the main downside of large sensor arrays can be bulkier and heavier helmets are less ideal for wearable MEG systems.

Overall, SERF sensors deliver better performance because they have lower intrinsic noise level than NMOR sensors in similar conditions. However, NMOR sensors can operate in higher magnetic field environment, have higher dynamic range and are more resilient to external field fluctuations. Furthermore, the vapour cell of SERF sensor needs to be heated to > 120°, while NMOR sensors work at room-temperature so the cell can be brought even closer to the scalp.

Note, that residual noise $\tilde{N}_r \geqslant 50$ fT eliminates both the advantage of SERF over NMOR and the advantage of large sensing volumes over small sensing volume in terms of the intrinsic noise level of the sensor. This effect is illustrated in Fig. 4 columns C and D. Furthermore, due to averaging the noises out both cell dimensions and the type of OPMs have little influence on localization accuracy (rows 3 and 4).

Our results highlight the role of brain noise, which dominates the residual noise present in a typical magnetically shielded room. Furthermore, we observed that a minimum of about 70 sensors are needed to reach the best localisation accuracy independent of the sensor's cell size and sensor type. This result is in line with the earlier hypothesis claiming that the sensor spacing should be comparable to noise correlation distance (Vrba and Robinson, 2002). Note that without the correlated brain noise included in the model the localisation accuracy is constantly improving with an increasing number of sensors (Beltrachini et al., 2021; Clancy et al., 2021; Vrba and Robinson, 2002).

Our model could be expanded to optimise any other parameter that was fixed in our numerical simulations, such as the intensity of the laser beam, the atomic density or the gap between the sensor and the head. In future work, it is also desirable to refine the signal and brain noise models. For example, one could replace the spherical head model with a more realistic brain-shaped model derived from an MRI scan. It would be also interesting to investigate arrays of tri-axial sensors that offer better intrinsic cancellation of the external noise sources (Brookes et al., 2021). However, in this case, a more sophisticated model for external noise is required. Ultimately, an actual recorded noise could be used to refine the optimal sensing volume dimensions.

[3] We have computed the lead field matrix from 1000 independent dipoles for an array of 69 sensors. For each sensor diameter we have computed a singular value decomposition of the lead field matrix and looked how the total spatial variability of a lead field is explained by such an array. The difference in the curves calculated for different sensor diameters were negligible in the considered range (2mm to 16 mm).

Declaration of Competing Interest

None

Credit authorship contribution statement

Yulia Bezsudnova: Investigation, Methodology, Software, Writing – original draft, Writing – review & editing. **Lari M. Koponen:** Investigation, Methodology, Software, Writing – review & editing. **Giovanni Barontini:** Conceptualization, Methodology, Resources, Funding acquisition, Writing – review & editing. **Ole Jensen:** Conceptualization, Methodology, Resources, Funding acquisition, Writing – review & editing. **Anna U. Kowalczyk:** Conceptualization, Methodology, Resources, Funding acquisition, Writing – review & editing, Project administration.

Data availability

The data and code presented here are available upon request to the corresponding author.

Acknowledgments

This work was supported by the BBSRC (grant number BB/R018723/1) and EPSRC (grant number EP/T001046/1). LK is supported by European Union's Horizon 2020 programme (No 101027633). OJ is supported by the Wellcome Trust Investigator Award in Science (grant number 207550) and the Royal Society Wolfson Research Merit Award. AK is supported by EPSRC Quantum Technology Career Development Fellowship (grant number EP/W028050/1). The computations described in this paper were performed using the University of Birmingham's BEAR Cloud service, which provides flexible resource for intensive computational work to the University's research community. See http://www.birmingham.ac.uk/bear for more details.

Appendix A

A.1. NMOR OPM sensor

We optimize the sensing volume dimensions of an NMOR sensor similar to (Kowalczyk et al., 2021), with an anti-relaxation coated vapour cell containing ^{87}Rb atoms. Without a buffer gas, the atoms can travel freely in the cell and the sensing volume is $V = L \times D^2$ where L is the cell length, D^2 is the cross-section of the cell (Fig. 1). For such a sensor, the atomic shot-noise limit originates from fluctuations of the number of atoms that contribute to the signal and it depends on the finite lifetime of the light-induced atomic polarization (Pustelny et al., 2008),

$$\delta B_{\mathrm{at}} = \frac{1}{\gamma}\sqrt{\frac{\Gamma}{nV}}, \tag{A.1.1}$$

Table A.1
Constants and parameters used in the model (1) (Zhao et al., 2015), (2) (Pustelny, 2007), (3) (Shah et al., 2007), (4) (Budker and Romalis, 2007), and (5) (Seltzer, 2008).

Common			
k_v	$1.12 \cdot 10^{-23}$ m^2 (1)		
ν_{laser}	377 THz		
P_{laser}	$7 \cdot 10^{-6}$ W		
f_{BW}	25 Hz		
ΔB	1 nT/m		
NMOR OPM (^{87}Rb)		**SERF OPM (^{87}Rb)**	
γ	$43 \cdot 10^9$ Hz/T	γ^e	$1.7 \cdot 10^{11}$ Hz/T (5)
n	$8.5 \cdot 10^{15}$ m^{-3}	n	$1 \cdot 10^{20}$ m^{-3}
I	3/2	I	3/2
T	295 K	T	450 K
A_{NMOR}	$0.6 \cdot 10^{-3}$ rad	σ_{SD}^{SERF}	$1.6 \cdot 10^{-21}$ m^{-2} (5)
σ_{se}	$2 \cdot 10^{-18}$ m^2 (3)	$\sigma_{sd}^{\mathrm{Ne}}$	$1 \cdot 10^{-28}$ m^{-2} (5)
C_w	10^{-4} (4)	$\sigma_{sd}^{N_2}$	$1 \cdot 10^{-26}$ m^{-2} (5)
		D_0	$0.2 \cdot 10^{-4}$ m^2/s (5)
		p_{Ne}	600 Torr
		p_{N_2}	20 Torr

where γ is the gyromagnetic ratio, Γ the half-width at half maximum of the NMOR resonance, and n the atomic density.

In NMOR magnetometers, the photon-shot noise is the leading contribution to the intrinsic noise. The polarization rotation noise per unit bandwidth due to quantum fluctuations is proportional to the number of photons in the probe beam N_{ph} as (Pustelny et al., 2008)

$$\delta B_{\mathrm{ph}} = \frac{1}{2\gamma}\frac{\Gamma}{A_{\mathrm{NMOR}}}\sqrt{\frac{1}{N_{\mathrm{ph}}}}, \tag{A.1.2}$$

where A_{NMOR} is the amplitude of NMOR resonance.

Both δB_{at} and δB_{ph} depend on the width of the resonance Γ, which is the inverse of the spin relaxation time (Pustelny, 2007). The width of the resonance is determined by the sum of several relaxation rates:

$$\Gamma = R_{se} + R_{wall} + R_{light} + R_{noise}, \tag{A.1.3}$$

where R_{se} is the spin-exchange collision relaxation rate, R_{wall} is the wall collision relaxation rate, R_{light} is the light-induced relaxation rate, and R_{noise} is the relaxation rate induced by external field fluctuation. The relaxation rate due to collisions between alkali atoms is given by

$$R_{se} = q(I)\sigma_{se}v_{rel}n, \tag{A.1.4}$$

where $q(I) = (6I+1)/(\pi \times (8I+4)))$ is the nuclear slow-down factor, I the nuclear spin of alkali atom, σ_{se} is the spin-exchange collision cross-section and $v_{rel} = \sqrt{2}v_{th}$ is the average atomic relative velocity with

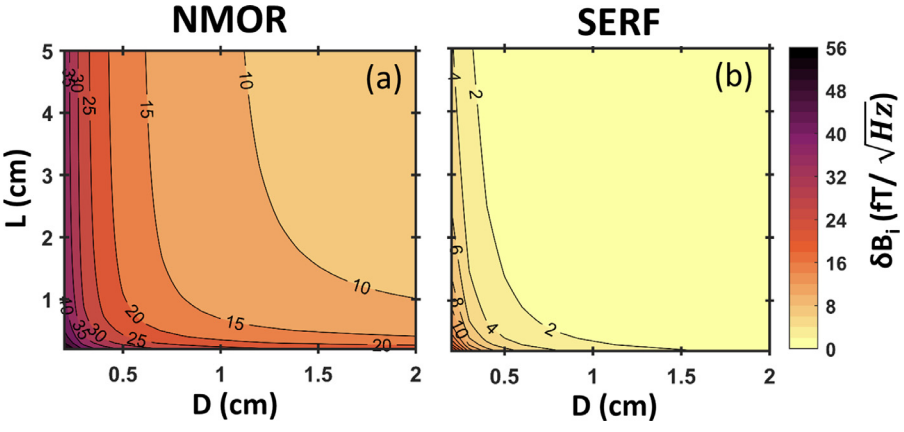

Fig. A1. OPM intrinsic sensor sensitivity δB_i as a function of L and D of the sensing volume for NMOR (a) and for SERF (b)

$v_{th} = \sqrt{8k_B T/m}$, where k_B is the Boltzmann constant, T the temperature of the gas and m the atomic mass.

The wall-collision-induced relaxation rate is given by:

$$R_{wall} = C_w \frac{1}{T_c}, \tag{A.1.5}$$

where C_w is the probability of electron spin relaxation during the collisions with the coating of the walls and $T_c = 4V/(v_{th} S_{cell})$ with S_{cell} as the surface area of the cell.

The light-induced relaxation rate is caused by the pump light (Budker and Romalis, 2007) and is due to transitions between Zeeman ground states. This rate is proportional to the average incident light intensity I_{mean}:

$$R_{light} = 2\frac{k_\nu}{\hbar \nu_l} I_{mean}, \tag{A.1.6}$$

where k_ν is the microscopic absorption cross-section, $\hbar$ the reduced Planck constant and ν_l the frequency of the pumping light.

Finally, spatial field fluctuations randomly shift the resonance frequency, resulting in a broadening of the magnetic resonance lines according to

$$R_{noise} = \gamma^2 (\Delta B)^2 \frac{L}{v_{th}}, \tag{A.1.7}$$

where ΔB is the root mean square of the magnetic field fluctuations over the length of the cell L. For a sensor similar to (Kowalczyk et al., 2021), ΔB is dominated by the bias field applied over the cell and is thus independent of the spatial fluctuations of measured signals.

A.2. SERF OPM sensor

We model a SERF OPM with a single-beam configuration similar to commercial sensors (Savukov et al., 2017). The vapour cell contains ^{87}Rb atoms, Ne as a buffer gas, and N_2 as quenching gas. For the optimal pumping rate, the atomic shot noise is given by (Budker and Romalis, 2007; Savukov et al., 2017)

$$\delta B_{\text{at}} = \frac{4}{\tilde{\gamma^e}} \sqrt{\frac{\Gamma}{nV}}, \tag{A.2.1}$$

where $\tilde{\gamma^e} = \frac{\gamma^e}{2I+1}$ and γ^e is the gyromagnetic ratio of a bare electron. V is the volume corresponding to the intersection of a laser beam with the vapour cell volume $V = L \cdot D^2$, where L is the cell length, D^2 is the laser beam cross-section area; and the photon shot-noise is

$$\delta B_{\text{ph}} = \frac{4\Gamma}{\tilde{\gamma^e}} \sqrt{\frac{1}{N_{\text{ph}}}}. \tag{A.2.2}$$

In the SERF magnetometer, spin-exchange relaxation is suppressed. The residual magnetic width Γ is due to spin-destruction collisions R_{SD}, collisions with the walls R_{wall}, the interaction with the light R_{pump}. With optimal pumping R_{pump} equals the sum of R_* caused by all other relaxation mechanisms. Overall the relaxation rate in SERF regime is expressed as:

$$\Gamma = R_{SD} + R_{wall} + R_{pump} + R_{noise}, \tag{A.2.3}$$

where the R_{SD} is the relaxation rate due to spin destruction is given by

$$R_{SD} = R_{SD}^{SERF} + R_{SD}^{B} + R_{SD}^{Q}. \tag{A.2.4}$$

Here the first term is due to collisions with other alkali atoms, the second term is due to collisions with buffer gas atoms, and the third term is due to collisions with quenching gas molecules. Each of these three terms can be written as

$$R_{SD}^{*} = \frac{1}{2I+1} n_* v_{rel} \sigma_{SD}^{*}, \tag{A.2.5}$$

where denotes relevant atoms, $v_{rel} = \sqrt{8k_B T/(\pi M)}$, $M = (1/m + 1/m')^{-1}$ with m alkali atom mass, m' the relevant atom mass, n_* is relevant atomic density.

The wall-collision-induced relaxation rate is given by

$$R_{wall} = D_0 \frac{p_0}{p} \left(\frac{2.4^2}{D^2} + \frac{\pi^2}{L^2} \right), \tag{A.2.6}$$

where D_0 is the diffusion constant of the alkali atom within the buffer gas, $p_0 = 760$ Torr, p is the buffer gas pressure.

The broadening due to magnetic field fluctuations are the same for SERF and NMOR, thus R_{noise} is obtained from Eq. A.7.

References

Acosta, V., Ledbetter, M.P., Rochester, S.M., Budker, D., Kimball, D.F., Hovde, D.C., Gawlik, W., Pustelny, S., Zachorowski, J., Yashchuk, V.V., 2006. Nonlinear magneto-optical rotation with frequency-modulated light in the geophysical field range. Physical Review A - Atomic, Molecular, and Optical Physics 73 (5), 1–8. doi:10.1103/PhysRevA.73.053404.

Ahonen, A.I., Hämäläinen, M.S., Kajola, M.J., Knuutila, J.E., Laine, P.P., Lounasmaa, O.V., Parkkonen, L.T., Simóla, J.T., Tesche, C.D., 1993. 122-Channel Squid Instrument for Investigating the Magnetic Signals From the Human Brain. Physica Scripta 1993 (T49A), 198–205. doi:10.1088/0031-8949/1993/T49A/033.

Barratt, E.L., Francis, S.T., Morris, P.G., Brookes, M.J., 2018. Mapping the topological organisation of beta oscillations in motor cortex using meg. NeuroImage 181, 831–844. doi:10.1016/j.neuroimage.2018.06.041.

Bell, W.E., Bloom, A.L., 1957. Optical detection of magnetic resonance in alkali metal vapor. Physical Review 107 (6), 1559–1565. doi:10.1103/PhysRev.107.1559.

Beltrachini, L., von Ellenrieder, N., Eichardt, R., Haueisen, J., 2021. Optimal design of on-scalp electromagnetic sensor arrays for brain source localisation. Human Brain Mapping 42 (15), 4869–4879. doi:10.1002/hbm.25586.

Borna, A., Carter, T.R., Colombo, A.P., Jau, Y.Y., McKay, J., Weisend, M., Taulu, S., Stephen, J.M., Schwindt, P.D., 2020. Non-invasive functional-brain-imaging with an OPM-based magnetoencephalography system. PLoS ONE 15 (1), 1–24. doi:10.1371/journal.pone.0227684.

Boto, E., Bowtell, R., Krüger, P., Fromhold, T.M., Morris, P.G., Meyer, S.S., Barnes, G.R., Brookes, M.J., 2016. On the potential of a new generation of magnetometers for MEG: A beamformer simulation study. PLoS ONE 11 (8), 1–24. doi:10.1371/journal.pone.0157655.

Boto, E., Holmes, N., Leggett, J., Roberts, G., Shah, V., Meyer, S.S., Muñoz, L.D., Mullinger, K.J., Tierney, T.M., Bestmann, S., Barnes, G.R., Bowtell, R., Brookes, M.J., 2018. Moving magnetoencephalography towards real-world applications with a wearable system. Nature 555 (7698), 657–661. doi:10.1038/nature26147.

Brookes, M.J., Boto, E., Rea, M., Shah, V., Osborne, J., Holmes, N., Hill, R.M., Leggett, J., Rhodes, N., Bowtell, R., 2021. Theoretical advantages of a triaxial optically pumped magnetometer magnetoencephalography system. NeuroImage 236, 118025. doi:10.1016/j.neuroimage.2021.118025.

Brookes, M.J., Vrba, J., Robinson, S.E., Stevenson, C.M., Peters, A.M., Barnes, G.R., Hillebrand, A., Morris, P.G., 2008. Optimising experimental design for MEG beamformer imaging. NeuroImage 39 (4), 1788–1802. doi:10.1016/j.neuroimage.2007.09.050.

Broser, P.J., Knappe, S., Kajal, D.-S., Noury, N., Alem, O., Shah, V., Braun, C., 2018. Optically pumped magnetometers for magneto-myography to study the innervation of the hand. IEEE Transactions on Neural Systems and Rehabilitation Engineering 26 (11), 2226–2230. doi:10.1109/TNSRE.2018.2871947.

Budker, D., Romalis, M., 2007. Optical magnetometry. Nature Physics 3 (4), 227–234. doi:10.1038/nphys566.

Clancy, R.J., Gerginov, V., Alem, O., Becker, S., Knappe, S., 2021. A study of scalar optically-pumped magnetometers for use in magnetoencephalography without shielding. Physics in Medicine and Biology 66 (17). doi:10.1088/1361-6560/ac18fb.

Colombo, A.P., Carter, T.R., Borna, A., Jau, Y.-Y., Johnson, C.N., Dagel, A.L., Schwindt, P.D.D., 2016. Four-channel optically pumped atomic magnetometer for magnetoencephalography. Opt. Express 24 (14), 15403–15416. doi:10.1364/OE.24.015403.

Deserno, M., 2004. How to generate equidistributed points on the surface of a sphere, 2004. XX. URL: https://www.cmu.edu/biolphys/deserno/pdf/sphere_equi.pdf

Duque-Muñoz, L., Tierney, T.M., Meyer, S.S., Boto, E., Holmes, N., Roberts, G., Leggett, J., Vargas-Bonilla, J.F., Bowtell, R., Brookes, M.J., López, J.D., Barnes, G.R., 2019. Data-driven model optimization for optically pumped magnetometer sensor arrays. Human Brain Mapping 40 (15), 4357–4369. doi:10.1002/hbm.24707.

Hämäläinen, M., Hari, R., Ilmoniemi, R.J., Knuutila, J., Lounasmaa, O.V., 1993. Magnetoencephalography-theory, instrumentation, and applications to noninvasive studies of the working human brain. Reviews of modern Physics 65 (2), 413.

Handy, T.C., 2005. Event-related potentials: A methods handbook. MIT press.

Hill, R.M., Boto, E., Rea, M., Holmes, N., Leggett, J., Coles, L.A., Papastavrou, M., Everton, S.K., Hunt, B.A., Sims, D., Osborne, J., Shah, V., Bowtell, R., Brookes, M.J., 2020. Multi-channel whole-head opm-meg: Helmet design and a comparison with a conventional system. NeuroImage 219, 116995. doi:10.1016/j.neuroimage.2020.116995.

Holmes, N., Rea, M., Hill, R.M., Boto, E., Stuart, A., Leggett, J., Edwards, L.J., Rhodes, N., Shah, V., Osborne, J., Fromhold, T.M., Glover, P., Montague, P.R., Brookes, M.J., Bowtell, R., 2021. Naturalistic hyperscanning with wearable magnetoencephalography. bioRxiv doi:10.1101/2021.09.07.459124.

Holmes, N., Tierney, T., Leggett, J., Boto, E., Mellor, S., Roberts, G., Hill, R., Shah, V., Barnes, G., Brookes, M., Bowtell, R., 2019. Balanced, bi-planar magnetic field and field gradient coils for field compensation in wearable magnetoencephalography. Scientific Reports 9. doi:10.1038/s41598-019-50697-w.

Iivanainen, J., Mäkinen, A.J., Zetter, R., Stenroos, M., Ilmoniemi, R.J., Parkkonen, L., 2021. Spatial sampling of meg and eeg based on generalized spatial-frequency analysis and optimal design. NeuroImage 245, 118747. doi:10.1016/j.neuroimage.2021.118747.

Iivanainen, J., Stenroos, M., Parkkonen, L., 2017. Measuring MEG closer to the brain: Performance of on-scalp sensor arrays. NeuroImage 147, 542–553. doi:10.1016/j.neuroimage.2016.12.048.

Iivanainen, J., Zetter, R., Grön, M., Hakkarainen, K., Parkkonen, L., 2019. On-scalp meg system utilizing an actively shielded array of optically-pumped magnetometers. NeuroImage 194, 244–258. doi:10.1016/j.neuroimage.2019.03.022.

Iivanainen, J., Zetter, R., Parkkonen, L., 2020. Potential of on-scalp MEG: Robust detection of human visual gamma-band responses. Human Brain Mapping 41 (1), 150–161. doi:10.1002/hbm.24795.

Jaiswal, A., Nenonen, J., Stenroos, M., Gramfort, A., Dalal, S.S., Westner, B.U., Litvak, V., Mosher, J.C., Schoffelen, J.-M., Witton, C., Oostenveld, R., Parkkonen, L., 2020. Comparison of beamformer implementations for meg source localization. NeuroImage 216, 116797. doi:10.1016/j.neuroimage.2020.116797.

Jensen, K., Budvytyte, R., Thomas, R.A., Wang, T., Fuchs, A.M., Balabas, M.V., Vasilakis, G., Mosgaard, L.D., Størkind, H.C., Müller, J.H., Heimburg, T., Olesen, S.-P., Polzik, E.S., 2016. Non-invasive detection of animal nerve impulses with an atomic magnetometer operating near quantum limited sensitivity. Scientific Reports 6 (1). doi:10.1038/srep29638.

Johnson, C., Schwindt, P.D.D., Weisend, M., 2010. Magnetoencephalography with a two-color pump-probe, fiber-coupled atomic magnetometer. Applied Physics Letters 97 (24), 243703. doi:10.1063/1.3522648.

Kamada, K., Sato, D., Ito, Y., Natsukawa, H., Okano, K., Mizutani, N., Kobayashi, T., 2015. Human magnetoencephalogram measurements using newly developed compact module of high-sensitivity atomic magnetometer. Japanese Journal of Applied Physics 54 (2), 026601. doi:10.7567/jjap.54.026601.

Kemppainen, P.K., Ilmoniemi, R.J., 1989. Channel capacity of multichannel magnetometers. In: Advances in biomagnetism. Springer, pp. 635–638.

Knappe, S., Alem, O., Sheng, D., Kitching, J., 2016. Microfabricated Optically-Pumped Magnetometers for Biomagnetic Applications. Journal of Physics: Conference Series 723 (1). doi:10.1088/1742-6596/723/1/012055.

Kowalczyk, A.U., Bezsudnova, Y., Jensen, O., Barontini, G., 2021. Detection of human auditory evoked brain signals with a resilient nonlinear optically pumped magnetometer. NeuroImage 226, 117497. doi:10.1016/j.neuroimage.2020.117497.

Krzyzewski, S.P., Perry, A.R., Gerginov, V., Knappe, S., 2019. Characterization of noise sources in a microfabricated single-beam zero-field optically-pumped magnetometer. Journal of Applied Physics 126 (4), 044504. doi:10.1063/1.5098088.

Marhl, U., Jodko-Władzińska, A., Brühl, R., Sander, T., Jazbinsek, V., 2022. Transforming and comparing data between standard squid and opm-meg systems. PLOS ONE 17, e0262669. doi:10.1371/journal.pone.0262669.

Marhl, U., Sander, T., Jazbinšek, V., 2022. Simulation study of different opm-meg measurement components. Sensors 22 (9). doi:10.3390/s22093184.

Oostenveld, R., Fries, P., Maris, E., Schoffelen, J.M., 2011. FieldTrip: Open source software for advanced analysis of MEG, EEG, and invasive electrophysiological data. Computational Intelligence and Neuroscience 2011. doi:10.1155/2011/156869.

Osborne, J., Orton, J., Alem, O., Shah, V., 2018. Fully integrated standalone zero field optically pumped magnetometer for biomagnetism. In: Shahriar, S.M., Scheuer, J. (Eds.), Steep Dispersion Engineering and Opto-Atomic Precision Metrology XI, International Society for Optics and Photonics. SPIE, pp. 89–95. doi:10.1117/12.2299197.

Pratt, E.J., Ledbetter, M., Jiménez-Martínez, R., Shapiro, B., Solon, A., Iwata, G.Z., Garber, S., Gormley, J., Decker, D., Delgadillo, D., Dellis, A.T., Phillips, J., Sundar, G., Leung, J., Coyne, J., McKinley, M., Lopez, G., Homan, S., Marsh, L., Zhang, M., Maurice, V., Siepser, B., Giovannoli, T., Leverett, B., Lerner, G., Seidman, S., DeLuna, V., Wright-Freeman, K., Kates-Harbeck, J., Lasser, T., Mohseni, H., Sharp, T., Zorzos, A., Lara, A.H., Kouhzadi, A., Ojeda, A., Chopra, P., Bednarke, Z., Henninger, M., Alford, J.K., 2021. Kernel Flux: a whole-head 432-magnetometer optically-pumped magnetoencephalography (OP-MEG) system for brain activity imaging during natural human experiences. Proc. of SPIE 11700, 162–179. doi:10.1117/12.2581794.

Pustelny, S., 2007. Nonlinear Magneto-Optical Effects. Jagiellonian University.

Pustelny, S., Wojciechowski, A., Gring, M., Kotyrba, M., Zachorowski, J., Gawlik, W., 2008. Magnetometry based on nonlinear magneto-optical rotation with amplitude-modulated light. Journal of Applied Physics 103 (6). doi:10.1063/1.2844494.

Riaz, B., Pfeiffer, C., Schneiderman, J.F., 2017. Evaluation of realistic layouts for next generation on-scalp MEG: Spatial information density maps. Scientific Reports 7 (1), 1–12. doi:10.1038/s41598-017-07046-6.

Sander, T.H., Preusser, J., Mhaskar, R., Kitching, J., Trahms, L., Knappe, S., 2012. Magnetoencephalography with a chip-scale atomic magnetometer. Biomed. Opt. Express 3 (5), 981–990. doi:10.1364/BOE.3.000981.

Sarvas, J., 1987. Basic mathematical and electromagnetic concepts of the biomagnetic inverse problem. Physics in Medicine and Biology 32 (1), 11–22. doi:10.1088/0031-9155/32/1/004.

Savukov, I., Kim, Y.J., Shah, V., Boshier, M.G., 2017. High-sensitivity operation of single-beam optically pumped magnetometer in a kHz frequency range. Measurement Science and Technology 28 (3). doi:10.1088/1361-6501/aa58b4.

Seltzer, S.J., 2008. Developments in Alkali-Metal Atomic Magnetometry. Dissertation 283.

Seymour, R.A., Alexander, N., Mellor, S., O'Neill, G.C., Tierney, T.M., Barnes, G.R., Maguire, E.A., 2021. Interference suppression techniques for opm-based meg: Opportunities and challenges. NeuroImage 118834.

Shah, V., Knappe, S., Schwindt, P.D., Kitching, J., 2007. Subpicotesla atomic magnetometry with a microfabricated vapour cell. Nature Photonics 1 (11), 649–652. doi:10.1038/nphoton.2007.201.

Sheng, J., Wan, S., Yifan, S., Dou, R., Guo, Y., Wei, K., He, K., Qin, J., Gao, J.-H., 2017. Magnetoencephalography with a cs-based high-sensitivity compact atomic magnetometer. Review of Scientific Instruments 88, 094304. doi:10.1063/1.5001730.

Taulu, S., Kajola, M., 2005. Presentation of electromagnetic multichannel data: the signal space separation method. Journal of Applied Physics 97 (12), 124905.

Tierney, T.M., Levy, A., Barry, D.N., Meyer, S.S., Shigihara, Y., Everatt, M., Mellor, S., Lopez, J.D., Bestmann, S., Holmes, N., Roberts, G., Hill, R.M., Boto, E., Leggett, J., Shah, V., Brookes, M.J., Bowtell, R., Maguire, E.A., Barnes, G.R., 2021. Mouth magnetoencephalography: A unique perspective on the human hippocampus. NeuroImage 225, 117443. doi:10.1016/j.neuroimage.2020.117443.

Van Veen, B.D., Van Drongelen, W., Yuchtman, M., Suzuki, A., 1997. Localization of brain electrical activity via linearly constrained minimum variance spatial filtering. IEEE Transactions on biomedical engineering 44 (9), 867–880.

Vrba, J., Robinson, S.E., 2002. SQUID sensor array configurations for magnetoencephalography applications. Superconductor Science and Technology 15 (9). doi:10.1088/0953-2048/15/9/201.

Westner, B.U., Lubell, J.I., Jensen, M., Hokland, S., Dalal, S.S., 2021. Contactless measurements of retinal activity using optically pumped magnetometers. NeuroImage 243, 118528. doi:10.1016/j.neuroimage.2021.118528.

Xia, H., Banranga, A.B.-A., Hoffman, D., Romalis, M., 2007. Detection of auditory evoked responses with atomic magnetometer. International Congress Series 1300, 627–630. doi:10.1016/j.ics.2007.02.028. New Frontiers in Biomagnetism. Proceedings of the 15th International Conference on Biomagnetism, Vancouver, BC, Canada, August 21-25, 2006

Zetter, R., Iivanainen, J., Stenroos, M., Parkkonen, L., 2018. Requirements for Coregistration Accuracy in On-Scalp MEG. Brain Topography 31 (6), 931–948. doi:10.1007/s10548-018-0656-5.

Zhao, M., Zhang, K., Chen, L.Q., 2015. Determination of the atomic density of rubidium-87. Chinese Physics B 24 (9). doi:10.1088/1674-1056/24/9/094206.